Multiscale characterization of dislocation development during cyclic bending under tension in commercially pure titanium

Nathan Miller[a], Nicholas Pitkin[b], Talukder Musfika Tasnim Oishi[b], Desmond Mensah[b], Marko Knezevic[b], Michael Miles[c], and David Fullwood[a*]

[a] Department of Mechanical Engineering, Brigham Young University, Provo, UT 84602
[b] Department of Mechanical Engineering, University of New Hampshire, Durham, NH 03824
[c] Department of Manufacturing Engineering, Brigham Young University, Provo, UT 84602

[*] Corresponding author e-*mail address*: dfullwood@byu.edu (D. Fullwood)

Abstract

Continuous bending under tension (CBT) has been shown to increase room temperature elongation-to-failure in various sheet metals beyond that of simple tension. A greater understanding of deformation mechanisms in CBT would allow for its elongation-enhancing effects to be more fully exploited, creating potential for new forming strategies. CBT-induced cyclic bending/unbending stresses combined with applied macroscopic tensile stresses create complex through-thickness stress profiles, where differing hardening behavior is expected near the surfaces compared with the middle of the sheet. This work uses high resolution electron backscatter diffraction characterization of geometrically necessary dislocation density together with X-ray diffraction-based evaluations of total dislocation density and in-plane digital image correlation to provide an in-depth analysis of through-thickness dislocation development and associated hardening rates throughout the CBT process in CP-Ti Grade 4 sheet metal. It was found that dislocation density is relatively uniform across the sheet at lower cycles, increases in the sheet center at higher cycles, and eventually approaches saturation near failure. Namely, dislocation accumulation occurs more slowly in the ratcheting, bending/unbending portions of the sheet (i.e., near the surfaces) from cyclic load reversals, and develops faster in the central tensile portion, where dislocation density up to 1.43x higher than near the surfaces was observed. High dislocation densities in the sheet center were found to precede significant central void accumulation, concentrating damage away from peak surface stresses, presumably contributing to delayed failure.

Keywords: dislocation density; elongation to failure; strain hardening; cyclic bending under tension; commercially pure titanium (CP-Ti); sheet metal forming

1. Introduction

Cyclic bending under tension (CBT) is a sheet metal forming test/process that has been shown to increase room temperature (RT) elongation to failure (ETF) of various metals beyond that of uniaxial simple tension (ST) [1, 2]. Examples of remarkable improvements in RT ETF over ST using CBT include: 5x, 4.5x, 3.7x, 2.5-3x, 1.5x, and 1.2-1.4x ETF in DP [3], Q&P, and TBF [4] 1180 steels, CP-Ti Grade 4 [5, 6], AA6022-T4 [2], and Mg alloys [7, 8], respectively, where the best material candidates for CBT are those that exhibit large necking in ST and relatively low hardening rates [5]. The process involves imposing a constant tensile strain rate on a given sheet while simultaneously bending it cyclically through a set of rollers (Figure 1) [9]. In CBT, strain localization (i.e., necking) is delayed as the sheet experiences *incremental* elongation about a moving deformation zone (i.e., continuous, spatially changing localized deformation) as opposed to *uniform* elongation through the gauge length [10, 11]. The greatest amount of plastic deformation occurs in the presence of combined macroscopic tensile stress and tensile stress from bending, where the bent area (i.e., deformation zone) changes incrementally with the passing rollers and preferentially experiences positive axial plastic strain [6, 10, 12]. This phenomenon occurs in conjunction with constant shifts in the location of the neutral axis, creating ratcheting (alternating) tensile and compressive bending/unbending regions toward the surfaces of the sheet as well as mainly pure (fluctuating) tension in the middle of the sheet (Figure 2) [4, 10, 13, 14].

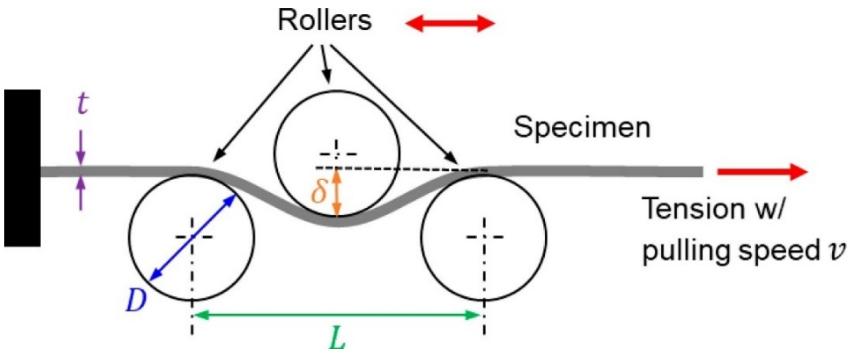

Figure 1. CBT process schematic including relevant process parameters (δ is bend depth). For the current test apparatus, bottom roller separation distance L is fixed at 54mm and roller diameter D at 25.4mm, with δ and ν variable. This image is from reference [5], used with permission.

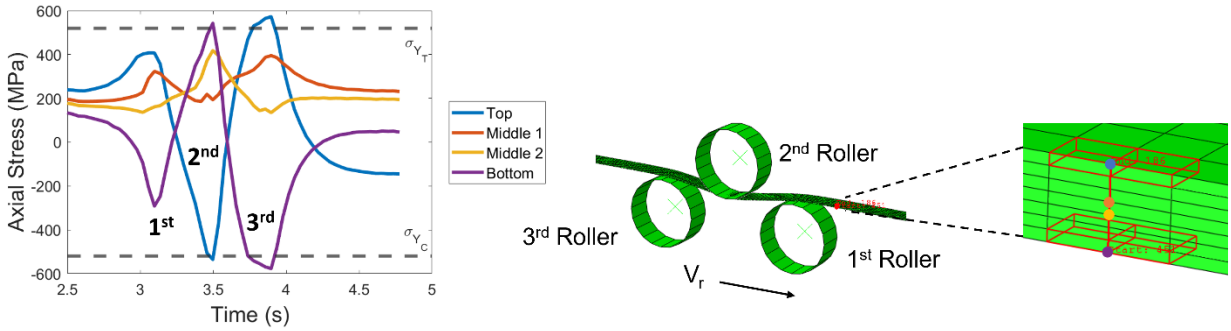

Figure 2. Axial stresses exhibited during the first CBT pass (0.5 cycles) for 4 of a line of 8 nodes within the 3x region. Contributions to elastic or plastic deformation of the 1st, 2nd, and 3rd rollers moving at relative velocity V_r are shown. Dramatic shifts between tension and compression near the surfaces and only tensile stresses in the sheet center are apparent. This figure assumes tensile-compressive yield stress symmetry.

In recent work, a test machine has been developed that grips a sheet metal sample, keeping it fixed at one end, bends it through three equally spaced rollers, and applies a constant tensile strain rate with a hydraulic cylinder on the opposite end [3]. The rollers are stationary in the axial direction but are allowed to spin freely. A carriage moves the specimen back and forth through the rollers for a desired number of cycles, or until failure [2, 11]. Key regions of interest in each specimen are distinguished by the number of rollers that the specimen passes through during each cycle, namely 1x, 2x, and 3x regions (Figure 3), where the 3x region is the standard CBT processing region. Key process parameters that govern material behavior and response during CBT are the normalized bend depth, pull speed (i.e., crosshead velocity), and carriage speed. The bend depth is the vertical displacement induced by the relative position of the middle roller, the pull speed is the tensile displacement rate induced by the cylinder, and the carriage speed governs the speed of the moving deformation zone. These parameters may be optimized to maximize the ETF of a given material, and said optimization correlates with the sheet thickness [5].

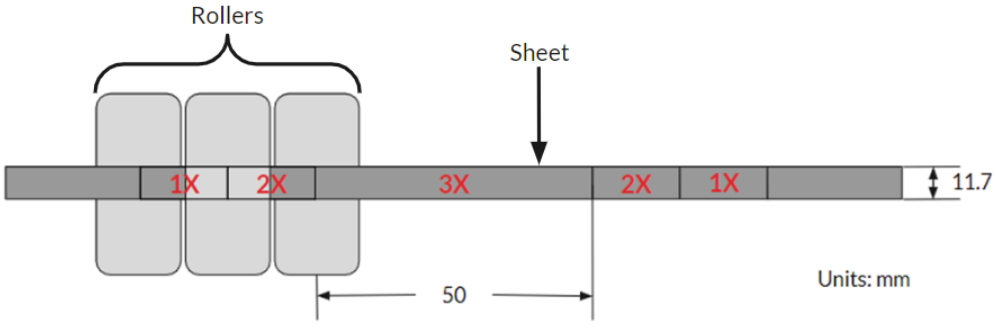

Figure 3. Regions of interest in the CBT process, distinguished by the number of rollers that pass through them, and initial specimen geometry of interrupted CBT specimens. This image is from reference [6].

It is of particular interest to exploit the CBT effects of enhanced ETF on HCP metals because of their desirable mechanical properties (such as strength-to-weight ratio) but limited

ductility during forming. Doing this may help circumvent traditionally low ductility, strong anisotropy, and limited active slip systems at RT that otherwise impede their more prevalent use in industry [15-18]. This work focuses on commercially pure titanium (CP-Ti) Grade 4 (highest strength, highest oxygen and iron content of Grades 1-4 [19, 20]), which serves as a promising candidate for CBT despite its hexagonal crystal structure due to its moderate formability and hardening, and substantial necking in uniaxial tension [5, 12]. CP-Ti Grade 4 is widely recognized as a noteworthy material for structural aerospace applications due to its high strength-to-weight ratio and excellent corrosion resistance. It can also be used more broadly to manufacture high-performance, lightweight components in aerospace, automotive, marine, energy, electronics, and health-care industries [18, 19, 21, 22]. Sheet fabrication of this metal via forming processes such as stamping and press forming is commonly performed at higher temperatures (i.e., superplastic forming) to facilitate greater part formability, but this can be costly. Heat treatments aiming to achieve a satisfactory net combination of strength and ductility also add significant cost. Using CBT to cold form CP-Ti sheets has the potential to increase the cost-effectiveness and efficiency of producing sheet metal parts. This is facilitated by eliminating furnace size restraints and typical surface cleaning used when hot forming, and mitigating use of potentially intensive heat treatments. A greater understanding of the micromechanical deformation mechanisms behind extended ETF from CBT in CP-Ti Grade 4 would provide applicable insights for using this process on other HCP metals and the broader spectrum of metals in general, creating potential for new forming strategies.

As was mentioned, CBT primarily enhances ETF by delaying localization (necking) via incremental deformation underneath the rollers. Stabilizing compressive stress profiles and relaxations of mechanical strain field fields are secondary causes of the improved elongation [12]. Behavior and distribution of microscale defect structures and damage accumulation contribute additional secondary effects within the microstructure, in addition to the structural effects. Thus, elucidating the mechanisms contributing to ETF improvements using CBT begins with determining an estimate of how much of the extra elongation is accounted for by delayed necking. This is done by comparing the maximum strain achieved at failure in the necked region of an ST sample with that of the failure region of a CBT sample. This assumes that the maximum strain achieved before failure in the necked region compared to the average strain in ST is the maximum strain achievable before failure by delaying localization. Digital image correlation (DIC) mapping from Sharma et al. [4] on transformation induced plasticity (TRIP) steels found that maximum strain across the 3x region in CBT was ~57%, and ~30% in the ST necked region, indicating that delayed localization only accounted for about half of the CBT-enhanced ETF. Previous DIC performed on the present material of this study, CP-Ti Grade 4, revealed a maximum local strain of ~36% in the ST necked region and ~45% in the 3x region near failure [6]. This indicates that in this material ~80% of the increase in ETF using CBT can be attributed to delayed localization. Both studies then suggested that important *secondary* deformation mechanisms explaining the ETF improvements are related to through-thickness damage evolution from the superimposed bending/unbending and tensile deformation behavior [4, 6]. Through-thickness analysis of defect structure development illuminates the localized nature of deformation arising from the cyclic nature of CBT. In the TRIP steel study, Sharma et al. [4] suggested that a proportion of the extended ETF stems, in part, from slower damage accumulation near the sheet surfaces due to repeated bending/unbending. They found that close to failure (at 10 out of 12 cycles) geometrically necessary dislocation (GND) accumulation in the center of a Q&P 1180 sheet was twice that of near-surface regions, potentially owing to

extensive dislocation reversal and annihilation from cyclic loading outside the pure tension zone. This is supported by their observations of the fracture surface and that dislocations accumulated 4x slower in CBT than in ST.

Knezevic et al. [23] were some of the first to physically observe and analyze intragranular dislocation cell structures in a material deformed by CBT: AA6022-T4. They tracked damage throughout the CBT process and compared it to damage accumulation in the necked region of failed ST samples. Using transmission electron microscopy (TEM), they observed dislocations tangles at 1 cycle (the material survived 8 cycles before failure), well-defined cells at 4 and 6 cycles, and no cell structures in the ST samples, finding only loose tangles and disorganized intragranular structures. They attribute this, in part, to the fact that substructure development is shown to be dependent on the strain level achieved, which is usually significantly higher in CBT, and that CBT deformation is more complex than that of ST owing to combined cyclic loading. Similar work was performed on DP 1180 steel. Yaddanapudi et al. [14] used TEM to compare dislocation structures observed in ST (at failure) and CBT (at 6 out of 9 cycles), where the former was scanned near the fracture surface. In the CBT sample they observed dislocation tangles exhibiting loop-like structures, which were attributed to CBT-induced increases in strength, and predicted to form into cells at higher cycles. In contrast, a similar lack of structure and/or tangles in the as-received and ST-deformed samples was observed.

These findings are supplemented by recent studies on the present material, CP-Ti Grade 4, that investigated microstructure and texture evolution, and damage accumulation in terms of voids. First, considering the idea that twinning and de-twinning may play a significant role in resultant ETF during cyclic deformation, as in AZ31 [7], Matukhno et al. [5] determined that tensile deformation in Grade 4 was dominated by prismatic slip activity, with twinning only playing a minor role. The latter is expected, since twinning systems for this CP-Ti grade have been shown not to significantly activate when subject to RT rolling operations [20]. They determined that a moderately strong as-rolled basal texture evolved such that compressive strain in the c-axis direction on a fraction of grains activated minor pyramidal slip. Elongated grains were observed in the pull direction, as well as some grain fragmentation due to the high strains achieved. An Abaqus finite element (FE) CBT simulation for this material allowed for investigation of developing stresses and strains throughout the CBT process at any cross section through the gauge length (details reported in [5, 12]). The constitutive model followed strain rate-independent von Mises plasticity theory (J_2) and assumes isotropic expansion of yield surfaces [9].

In another study, Pitkin et al. [6] conducted an in-depth through-thickness investigation of void content and growth using X-ray computed tomography (XCT) to compare rates of damage accumulation in CBT compared to ST. They found that voids formed at similar rates with respect to local strains in both processes, but that CBT appeared to delay coalescence and accumulated significantly more voids before failure. The density of voids close to failure for both CBT and ST was highest in the sheet center. They suggested that the compressive force of the rollers, especially that of the middle roller, causes some local void closure in the material directly underneath it. Additional void closure was afforded to ratcheting compression from bending/unbending near the surfaces. Finally, stress relaxation outside of the current point of plastic deformation mitigated risk of voids external to it causing failure. All of these factors allowed for more strain (delayed coalescence) to be achieved in CBT. Once again, they proposed that a significant mechanism contributing to extended ETF in CBT is dislocation evolution,

where dislocations and/or structures are annihilated near the sheet surfaces during reverse loading.

Movement, annihilation and/or accumulation of dislocations is the primary mechanism of plastic deformation in polycrystalline metals [24, 25]. Previous work has revealed evolution of observed dislocation structures, texture, and void content, with hypotheses surrounding dislocation involvement in delayed failure. To connect these studies, an in-depth through-thickness investigation of the role and development of dislocations through a given sheet's cyclic lifetime is needed to better understand defect structures and damage accumulation during CBT, thereby explaining secondary mechanisms related to enhanced ETF. This study combines multiple characterization techniques to illuminate the interrelated contributions from slip system activity, associated hardening rates, and through-thickness dislocation evolution in the sheet. It is hypothesized that damage (i.e., accumulation of dislocations and voids) occurs more slowly in the ratcheting portions of the sheet (i.e., near the surfaces), thus delaying failure. High resolution electron backscatter diffraction (HR-EBSD) characterization of *GND* density, together with X-ray diffraction (XRD)-based evaluations of *total* dislocation density (totalDD), are combined with in-plane DIC and FE simulation prediction to better understand mechanisms for deformation behavior. Total dislocation and GND densities through the sheet thickness in two regions of interest within the gauge length are reported as a function of cycle number, progressively toward failure. Results are compared with dislocation populations developed during ST and previously reported void formation behavior to assess overall rates of through-thickness damage accumulation.

2. Experimental Procedures

2.1 General Sample Preparation

1mm-thick CP-Ti Grade 4 sheets were obtained from Boeing, having a nominal composition of 99.97% pure α-titanium. Strength and ductility properties of the as-received material were previously obtained, where the transverse direction (TD) relative to rolling was found to be the strongest sheet direction (Figure 4) [12].

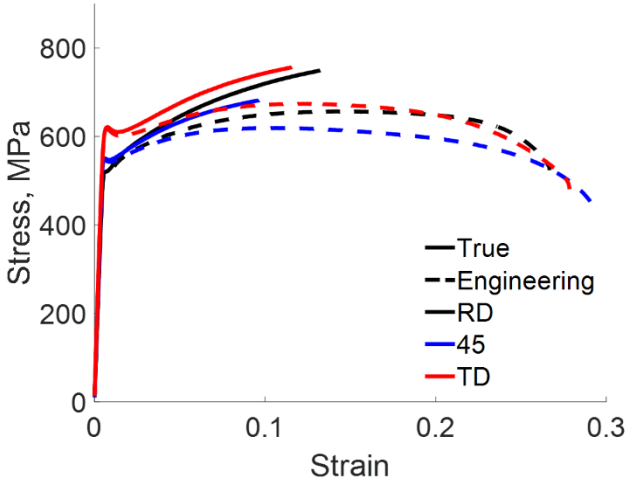

Figure 4. Strength and ductility characterization of as-received CP-Ti Grade 4 sheets. This image is from reference [12].

All CBT test specimens were cut from the sheet parallel to the rolling direction (RD) using a Flow waterjet cutter. Since CBT test specimens consistently fail at the 2x/3x interface, wider end grips were foregone and shorter (241mm long), rectangular (11.7mm wide) specimens were used to increase versatility for through-thickness polishing and potential in-situ imaging. The specimen length was maintained such that the 3x region was initially 50mm (Figure 3). Optimal machine process parameters (i.e., $v = 1.3$ m/s and $\delta = 3.5$mm, and carriage speed 66 m/s [Figure 1]) were used to analyze best-case enhanced ETF [5, 6]. For the CBT experiments the major strain direction was imposed along the RD. Under this specimen geometry and test parameters, CP-Ti Grade 4 specimens tend to fail just after completing ~12.5 cycles [6], where one cycle is defined as the specimen passing through the rollers once in both directions as the carriage traverses back and forth. Therefore, to analyze dislocation development over a range of different strain levels, cycle numbers investigated were 0 (undeformed), 0.5 (one pass), 1 (two passes), 8, and 12 (right before failure). CBT tests were carefully *interrupted* at each of these points at the end of a given cycle or half-cycle, and specimens removed, such as to preserve statistical equivalence as if from a single sample. A CBT test taken to failure is shown in Figure 5 with interrupted cycle numbers shown. Corresponding percentage ETF (i.e., ratio of elongation achieved to elongation at failure) obtained from interrupted testing for 0.5, 1, 8, and 12 cycles were 2.03, 5.36, 58.71, and 97.80%, respectively, where 100% represents failure of a given specimen.

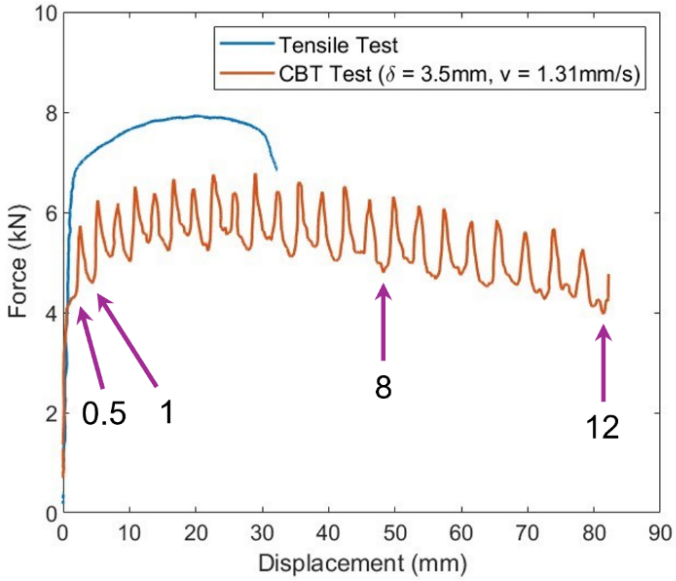

Figure 5. Load-displacement curve of CP-Ti Grade 4 up to ~12.5 cycles at optimal process parameters. The ETF of the sheet in ST was 32.3mm, and 82.2mm that of CBT, enhanced approximately 2.5 times. Cycle numbers interrupted and analyzed in this study are superimposed, where %ETF of interrupted tests would be statistically similar to corresponding instantaneous %ETF during a full CBT test to failure. This image is adapted from reference [6].

In terms of experimental design, 0.5 and 1 cycles were chosen to directly analyze the cyclic nature of CBT between passes, and 8 and 12 to further examine the progression of strain

hardening, dislocation saturation, and strain localization leading up to failure. For each cycle number (except in the undeformed case) in its interrupted state, one sample was cut from two regions of interest: the 1x/2x interface (under the middle roller) and 3x region (middle of the sheet). This was done using a diamond wet saw cutter to minimize further plastic deformation. The former region captures the location where the sheet stresses are expected to be at a maximum (i.e., in a resting bent state), presumably corresponding to high dislocation content, and is representative of the dislocation evolution under the roller along the moving deformation zone. The latter region captures the net dislocation evolution in the processing region of the sheet and the unbending effects of CBT, since what was once instantaneously bent becomes unbent as the specimen passes completely through the rollers. A sample was also cut from the as-received material, making 9 total samples. For distinguishability in this paper, the two main regions of interest will be referred to as "bent" and "unbent." Comparing these two areas can provide insight into the content of dislocations at key stress states and locations during the CBT process and their influence in enhancing RT ETF. The TD (strongest direction) face of extracted samples was analyzed with EBSD, and the normal direction (ND) face with XRD. Sample preparation is hereafter divided into two sections according to characterization method, followed by descriptions of other experimental methods.

2.2 HR-EBSD

After diamond-cutting, samples were embedded, TD upward, in epoxy resin, mechanically polished at grits of 320, 400, 600, 800, and 1200, removed from the epoxy, and subsequently electropolished in a 95% methanol, 5% perchloric acid ($HClO_4$) electrolyte solution: 25 V, 60 s, -30 °C < T < -21 °C. A vertical 316 stainless steel sheet served as the negative electrode. Post-polishing, samples were loaded into an Apreo C Low-Vacuum SEM, with a beam current of 3.2 nA and accelerating voltage of 20 kV. Thin EBSD scans of 20µm × Thickness (~1000µm, or 1mm), 0.5µm step size, and 2×2 binning were taken across the entire sheet thickness one each for 0.5, 1, 8, and 12 cycles in both the bent and unbent regions, and patterns saved (Figure 6). For bent region samples, scans were taken at the location of maximum bending curvature, which was easily identifiable from stage tilt distortion. Scan location in the unbent samples was arbitrary. Note that thickness of the sheet reduces as a function of strain, so the scan length generally decreased with cycle number. For the case of the undeformed sample, a square area of 120µm × 120µm was scanned (~136 grains). The grain size was between 8µm and 14µm on average.

Figure 6. Uncleaned EBSD scan at 0.5 cycles in the 3x region taken across the entire sheet thickness. The left side is the bottom of the sheet. Noise on the right side represents the end of scannable material.

GND density (total dislocation length per unit volume, units of m^{-2}) was calculated using HR-EBSD via Open-XY, where every scanned point is assigned a GND density value based on cross-correlation of lattice strain from neighboring points/patterns [26-28]. GND density values corresponding to points having a confidence index of less than 0.1, as defined by EDAX OIM

software, were filtered out. Inverse pole figure and corresponding GND density maps for each sample are shown in Figures A.1 and A.2 in the Appendix.

It should be noted that camera binning and resolution, sample preparation, and step size all play a large role in relative noise of GND calculations [29, 30]. Some corrosive pitting was observed on the scanning surface due to the electropolishing method used in sample preparation, contributing some noise to the calculations as it technically represents additional deformation to the sheet. Smaller step sizes predict fewer like-signed (polar) dislocations, and thus inflate the "true" GND density, classifying more dislocations as geometrically necessary. In essence, smaller step sizes increase noise and scan time, and larger step sizes exhibit some net dislocation cancellation and lower spatial resolution [30]. 0.5μm was ultimately chosen as the experimental step size, a common value used in HR-EBSD experiments for similar grain sizes, to preserve spatial resolution integrity of the microstructure, minimize time required for each scan, and avoid excessive noise in the data. Since the step size, sample preparation methods, approximate scan size, and equipment settings used were all kept *consistent*, results and trends are considered sound above a base noise floor.

After GND density was calculated for every point in the scan, the data was transformed to compute an average GND density from the 40 points (20μm wide, 0.5μm step size) at each step across the thickness, constructing an average dislocation gradient through the sheet. To filter out additional noise and determine the underlying trend of the data, the GND density was then calculated for 10 windows through the thickness of the sheet by dividing a given scan into 10 slices of equal size in the through-thickness direction and performing a window average of each slice.

2.3 XRD

Square samples with a side length of 5mm were cut from the same regions and indicated cycle numbers as previously mentioned, including the unstrained material, adhered to sample holders, ND upward, and loaded into a diffractometer together with a silicon standard powder sample. A P-XRD PANalytical X'Pert Pro MPD diffractometer having a Cu X-ray source, X'Celerator detector, and Ge monochromator tuned to the Cu-$K\alpha_1$ wavelength ($\lambda = 1.5406$ Å) was used to scan each sample. Samples were scanned in batches across multiple sessions. When a new batch was scanned, the Si standard was likewise scanned in the same session to provide an accurate reference for the current batch of titanium samples. Data was collected for the CP-Ti samples between 34° and 143° 2θ at a 0.0042° step size and counting time of 600.08 s/step (~34 hours overall). The Si standard was scanned between 20° and 120° 2θ at a 0.0042° step size and counting time of 55.88 s/step (~3 hours overall). To obtain a similar through-thickness dislocation gradient to compare to the HR-EBSD, three scans were taken for each sample, excepting the unstrained sample, beginning at the bottom surface of the sheet (in tension relative to the middle roller) separated by ~134 μm on average into the sheet thickness. Again, the scans were performed on the ND of each sample. The surfaces for the first scan were consistently not polished due to the curvature of the bent region samples. Following the surface scan for each sample, a hand polisher was used to grind each sample down twice, and an optical microscope used to measure thickness between each scan and corresponding removal of material. The TD face of the sheet was too thin and the inherent scanning area too large to scan along the edge, like in the EBSD case. Therefore, the ND was used, and a dislocation gradient constructed by stepping through the thickness, where trends are expected to be similar between ND and TD dislocation development despite material anisotropy. The maximum X-ray penetration depth at

90° 2θ was estimated to be 26μm, such that the diffraction data taken at each "plane" (surface, 1st shave down, 2nd shave down) was considered representative of the dislocations in the immediate scan area at that location through the thickness.

With data collected, the diffraction peaks were then post-processed using Convolutional Multiple Whole Profile (CMWP) fitting [31]. First, the background was subtracted from the Si standard scans, and instrument profiles obtained by isolating the Si peaks. Ti peaks were identified and paired with corresponding *hkl* indices recorded in the International Center for Diffraction Data (ICDD) database. Raw intensity data and Ti and Si peak data were subsequently run in CMWP and cycled through two sequences of consecutive Monte Carlo (MC) and Marquardt-Levenberg (ML) fits. A contrast factor, $\overline{C}_{hk.0}$, of 0.25 and burgers vector 0.295nm were used [32]. In the MC fit, the program ran until a set number of iterations (100 in this case) had reached a minimum weighted sum of squared residuals (WSSR) value below a certain confidence parameter threshold (set to 3.5% above the minimum) in the parameter space. Bounds of uncertainty were then the positive and negative percentages of the converged value corresponding to where the parameter space crosses that threshold, where a narrower minimization space would represent more confidence in the converged value. TotalDD, ρ (units of m^{-2}), output was considered satisfactory when there was negligible difference between the MC and ML fit results. Finally, the dislocation densities were run through two HCP-specific refinement programs/solvers [32] to extract refined totalDD values, the one reported being that which had the smallest least-squares minimization value between the solvers.

2.4 DIC

Relative strain hardening rates between specimens deformed both in ST and CBT were obtained by comparing HR-EBSD GND calculations to true strain mapped with DIC. Samples in ST and CBT were taken to failure while DIC was simultaneously performed on the ND surface to obtain respective 2D major strain profiles. DIC for the CBT sample was previously collected/reported in [6]. The true strain in the 3x region at %ETF corresponding to 0.5, 1, 8, and 12 cycles was directly compared to GND density in the 3x region for the same cycle numbers (Section 2.2). Only the 3x region was compared because of visual obstruction from the rollers at the 1x/2x interface. ST DIC from this study was obtained by first applying a polymer-based black and white spray paint speckle pattern to the tensile specimen. A 2-megapixel IMPERX B1921 HD camera was used to collect one image per second during the ST test, the specimen surface being illuminated by an LED light. Strain was mapped in Correlated Solutions® VIC-2D. ST specimens were interrupted also at %ETF corresponding to 0.5, 1, 8, and 12 cycles in CBT (i.e., 0.5: 2.03%; 1: 5.36%; 8: 58.71%; 12: 97.80%). Samples were subsequently cut and HR-EBSD performed in the TD in the middle of the necked region, near the necked region, and at several lower-strain locations between specimens to collect a wide range of true strain and corresponding GND density values.

2.5 Simulated Stress Profiles

To compare GND accumulation through the thickness of the sheet relative to the ratcheting, alternating stress (cyclic bending/unbending) regions of the sheet, outputs from the FE model were employed to track shifts in the neutral axis using axial stress profiles. Eight nodes were simulated through the sheet thickness (Figure 2). Cross sections for axial (σ_{11}) stress profiles were taken at locations of maximum bending curvature at two of the rollers and in the 3x region, at the surface of the sheet edge in the width direction, when the rollers had come to the end of the

indicated cycle number (to directly simulate experimental data). The cross sections for 3x, left roller, and middle roller are labeled 3x, TC1, and TC2, respectively, shown in Figure 7. With each passing roller, the bending state changes from positive bending, to negative, and back to positive, or vice versa. Thus, alternating compression-to-tension and tension-to-compression shifts were obtained by finding the through-thickness location where the axial stress profile changed sign. Neutral axis shifts in the 3x region were not relevant since it is not in a state of bending, but the profiles still serve as a reference. Axial plastic strain for each cross section was also obtained as an indicator of relative slip activity.

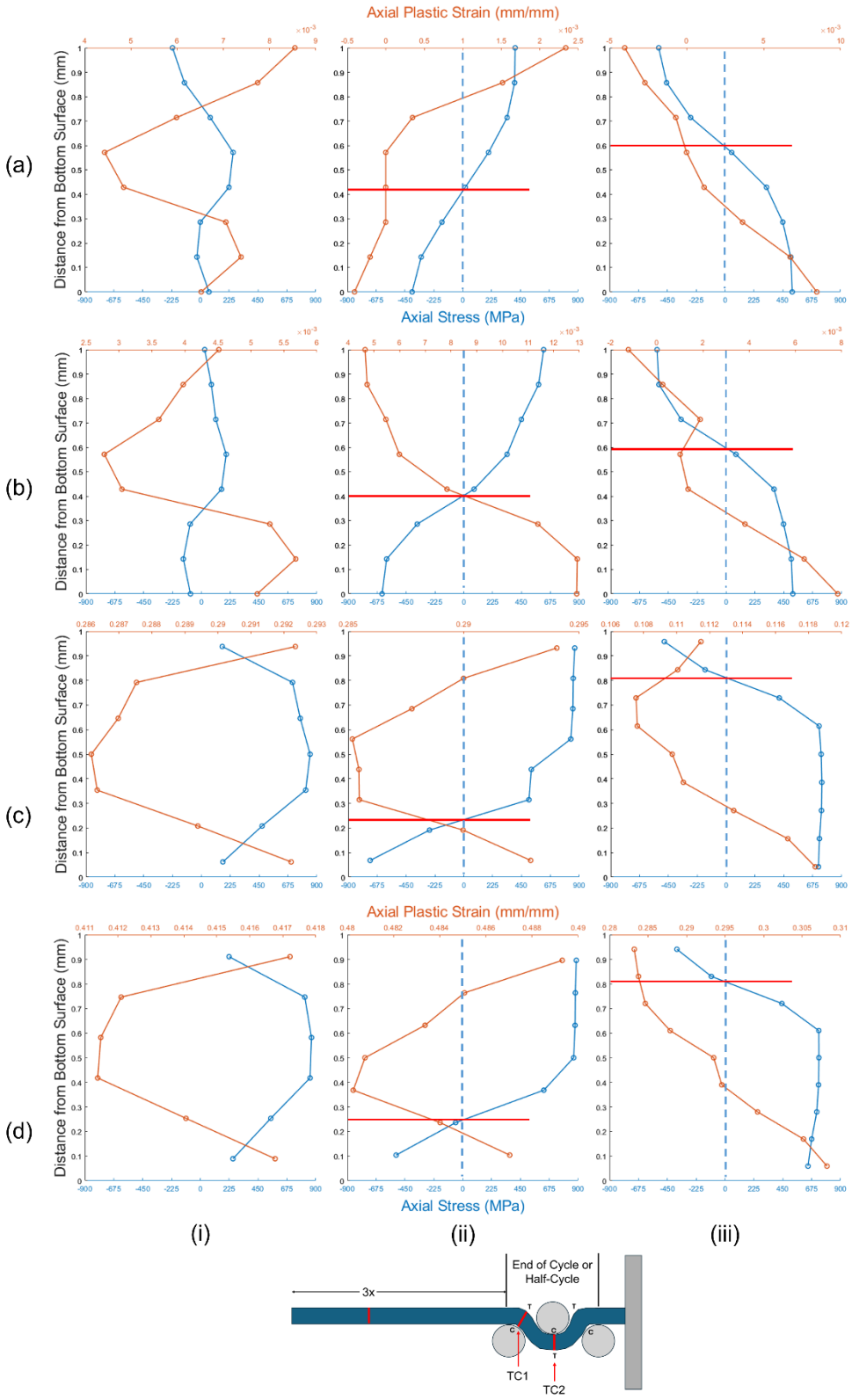

Figure 7. Simulated through-thickness axial stress and plastic strain profiles calculated at 8 nodes through a CP-Ti Grade 4 sheet at the end of (a) 0.5, (b) 1, (c) 8, and (d) 12 cycles at (i) 3x, (ii) TC1, and (iii) TC2 cross sections. The through-thickness location of shifting from negative to positive stress is indicated by the red lines.

3. Results & Discussion

3.1 Through-thickness HR-EBSD dislocation evolution analysis

The resultant alternating and constant-tension deformation zones estimated from FE simulations are shown in Figure 8, revealing regions of pure tensile stress in the middle, and ratcheting compressive and tensile stresses toward the surfaces. At lower cycles, the tension region covers ~20% of the thickness, and grows to ~60% at higher cycles. As the sheet gets thinner, the amount of compression that can be induced in the sheet is reduced. This gradually introduces more overall tensile stress in the middle of the sheet, shown at 8 and 12 cycles, accelerating failure. Thus, axial compressive stress serves as a stabilizing mechanism during CBT [5]. Overall, varying amounts of damage accumulation are expected between the differing deformation zones since they undergo different stress states and subsequent strain paths.

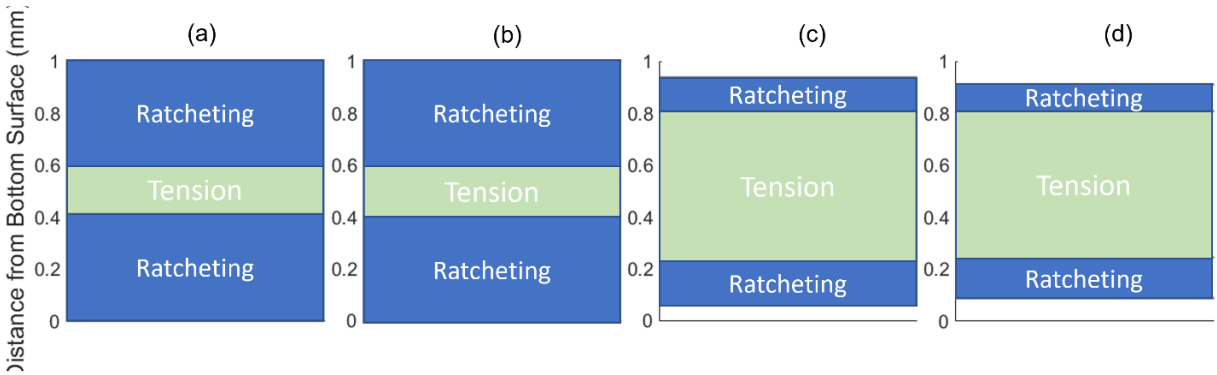

Figure 8. Through-thickness tension and alternating tension-compression regions at (a) 0.5, (b) 1, (c) 8, and (d) 12 CBT cycles. Each "snapshot" represents the tension-ratcheting distribution at an infinitesimal location at the end of the indicated cycle, with (gradually reducing) thickness estimations taken from the middle of the 3x region.

GND density accumulation under the middle roller (TC2, bent region, Figure 7) across the through-thickness of the sheet is shown in Figure 9. Recall that this region was analyzed to track dislocation development representative of immediate deformation under one of the rollers, whereas the unbent (3x, processing) region focuses on the net deformation from bending and unbending the sheet. First, a general increase in GND density is observed leading up to failure. Additionally, in this region GND density is shown to be generally highest at the bottom surface, which, under the middle roller, is bent in tension. Recall that the CBT tests were interrupted at the end of an indicated experimental cycle number (i.e., when the carriage had decelerated and come to a stop). Thus, the bias in dislocation density toward the bottom of the sheet is expected due to constant tensile strain applied at longer time intervals at the end of a pass (i.e., during the pause before beginning the next pass) in the presence of combined static tensile bending. This is in contrast to instantaneous locations in the processing (3x) region, where combined applied macroscopic tension and tensile bending at *constant velocity* are induced for fractions of a second as each roller passes. Note that tension from bending compounded with macroscopically applied tension induces the highest stresses and, hence, the greatest plastic deformation during the process [6, 12]. In short, more strain hardening was observed at the bottom surface of the sheet, indicating higher GND accumulation near the bottom surface throughout the CBT process at the end of each pass from (relatively) extended superimposed static tensile loading.

From the bent region results it is also noted that during the first cycle (0.5 and 1 cycles, 1st and 2nd pass), dislocation content is distributed linearly through the sheet (highest at the bottom surface). At 8 cycles, dislocation content is lower near the sheet surfaces and peaks in center, following a more quadratic distribution with respect to depth, indicating slowed accumulation in the ratcheting regions. Quantitatively, the GND density in the sheet center is approximately 1.43x higher than at the surfaces. In contrast, at 12 cycles dislocations are once again distributed more linearly through the sheet, rather than quadratically (once again highest at the bottom surface) indicating that dislocation density is approaching *saturation* throughout the sheet. In other words, hardening has been exhausted in certain areas of the sheet, and dislocations are annihilating each other. Saturation can be thought of as steady-state deformation behavior where the multiplication rate of dislocations is equal to the annihilation rate, or when none are being generated [33, 34]. The minor increase in GND density in the middle of the sheet between 8 and 12 cycles indicates that the central zone is more saturated, leading to more accumulation near the surfaces after 8 cycles. These results are generally consistent with data obtained from the unbent region, shown in Figure 10.

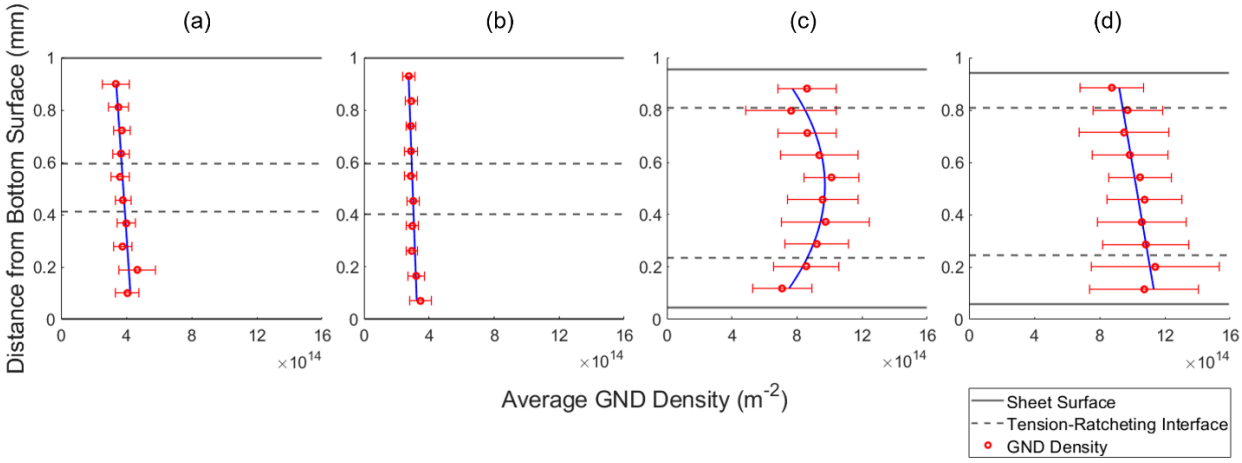

Figure 9. Average GND density and standard deviation of 10 slices of the data relative to through-thickness deformation zones (ratcheting, tension, ratcheting, separated by dotted lines) in the bent region at each experimental cycle number: (a) 0.5 cycles, (b) 1 cycle, (c) 8 cycles, (d) 12 cycles. Least square fits are also superimposed.

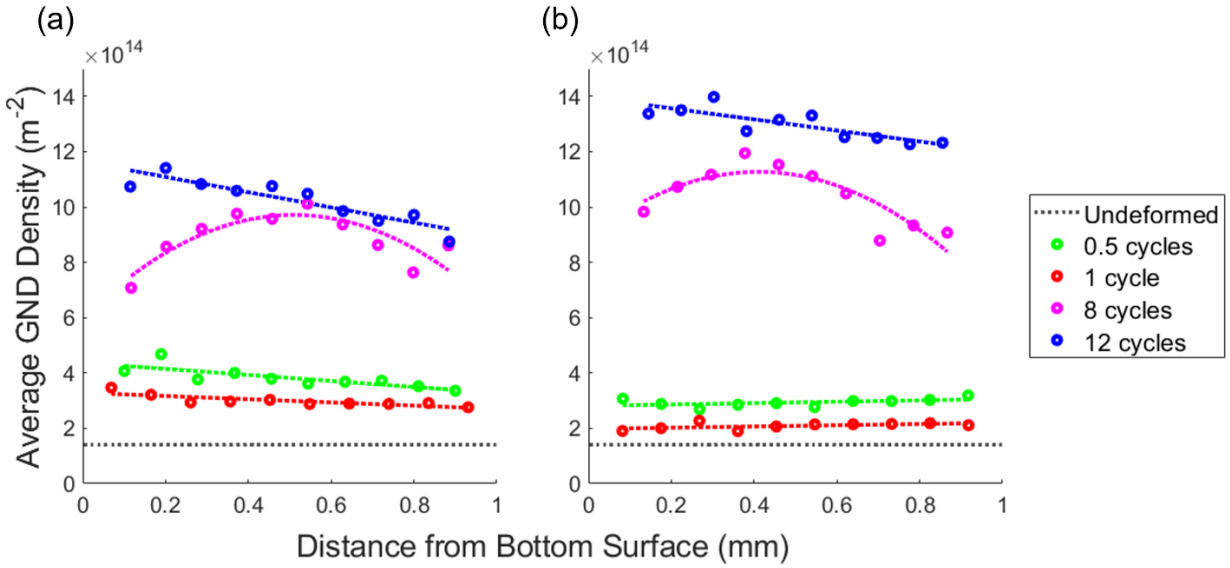

Figure 10. GND density accumulation in the (a) bent region and (b) unbent region superimposed with linear fits for 0.5, 1, and 12 cycles, and a quadratic fit for 8 cycles. Data for each cycle is centered at 0.5mm (half the sheet thickness), indicating a decrease in thickness over time.

Here, the dislocation content in the sheet center is 1.22-1.32x higher than at the surfaces after 8 cycles. After 12 cycles, a net higher accumulation near the bottom surface is observed, most likely due to top-to-bottom roller configuration asymmetry (i.e., one top roller and two bottom rollers).

It is curious that in both regions of interest from which data is taken for Figure 10, the GND density at 0.5 cycles was slightly higher than that at 1 cycle. However, these were two different samples, and sensitivity to initial test conditions is highest during the first few cycles. Hence the discrepancy is likely due to slightly different initial machine conditions (e.g., initial tension in the sample after the grips are applied); or there may be other factors such as cutting and polishing conditions.

As can be seen from Figure 10, at a low number of cycles dislocations accumulate between 30-40% faster in the regions at the 1x/2x interface in the 'bent' condition (Figure 10a), compared with the 'unbent' 3x region (10b). Presumably, a certain amount of dislocation annihilation occurs during the unbending of the sheet as the final roller passes over it. At higher cycles, however, plastic strain accumulates much faster in the 3x region, compared with the 1x/2x region [6], leading to higher dislocation content (compare the 8- and 12-cycle data in Figure 10b, compared with 10a).

3.2 Strain hardening comparison between CBT and ST

As was briefly mentioned, it was previously shown that GND density increases 4 times faster in ST than in CBT in TRIP steels, with near-linear hardening [4]. This finding was used to explain a related observation that GND density was 1.56x higher in the center of a Q&P 1180 sheet (at 10 out of 12 cycles) than near the surfaces, a similar trend to what was reported above for the CP-Ti. The strain state/paths in CBT are complex, exhibiting pure tension in the middle of the sheet and cyclic tension-compression combined with pure tension near the surfaces. Since the rate of GND

accumulation was found to be higher in ST, the GND density is expected to be, and was, higher in the middle of the sheet later in the deformation process. The GND accumulation was correspondingly slower in the ratcheting regions. A similar comparison of hardening rates between ST and CBT is corroborated in this study. Figure 11 shows hardening rates in CP-Ti using true strain data obtained from DIC superimposed with GND density obtained in the 3x region in CBT and throughout the gauge length in ST, including the necked region.

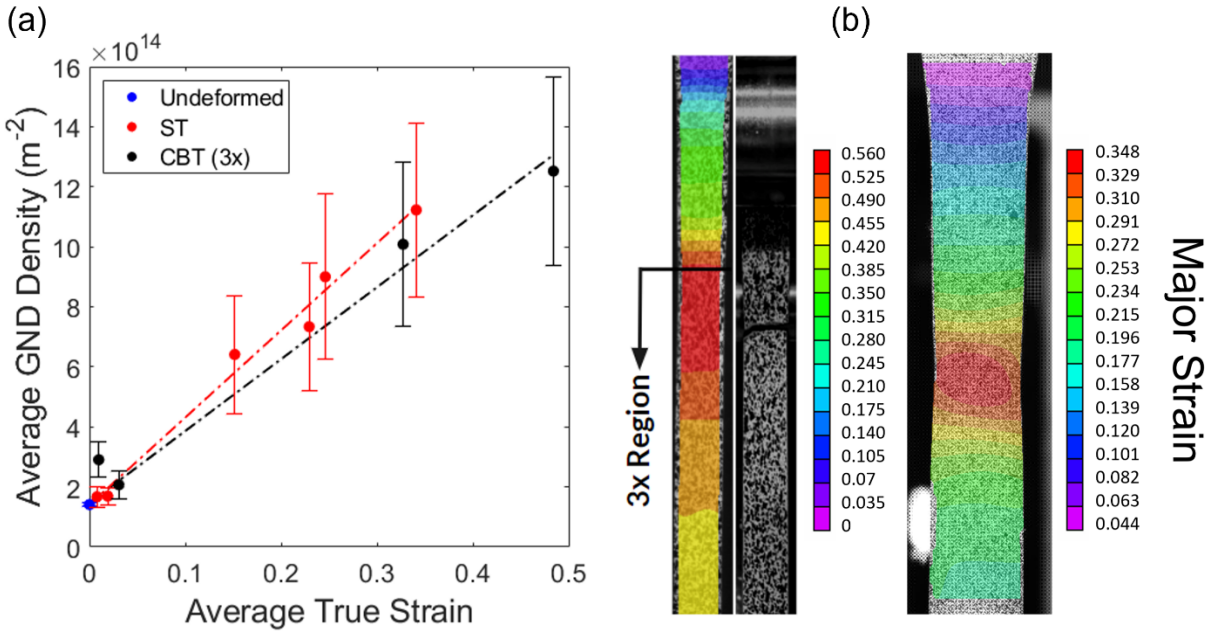

Figure 11. (a) Average strain hardening rates in ST compared to the CBT 3x region with (b) a sample of strain maps from corresponding DIC: CBT at failure (left), ST at 97.80% ETF in the necked region, just before failure (right). Error of one standard deviation from the mean is shown. Both linear models start with zero strain and corresponding GND density of the as-received material.

Simple linear regression was performed on the two datasets, giving R^2 values of 0.987 and 0.988 for CBT and ST, respectively. Thus, dislocations were found to develop 1.2 times slower in CBT than in ST in CP-Ti Grade 4 – a similar trend to the steel study, though not as pronounced. One possible explanation for a general discrepancy in hardening between CP-Ti and the Q&P/TBF 1180 is the number of phases present. In the TRIP steels, there is likely a greater tendency for higher localization and dislocation development around hard phases (i.e., greater hardening in one phase over another), as they have ample amounts of martensite and retained austenite [35, 36]. CP-Ti, on the other hand, only has one phase at RT.

3.3 Through-thickness CMWP dislocation evolution analysis

The totalDD data from CMWP serves as a companion to the HR-EBSD GND density data and reveals additional insights regarding damage accumulation. Data collected at the surface was discarded, being unreasonably high due to heavy damage from CBT surface rolling, not being polished, and/or (in the bent region) poor diffracted X-ray detection as a result of inherent curvature. Internal measurements were reasonable and overall considered to be sound. Through-

thickness totalDD computed in CMWP is displayed in Figure 12. Anomalistic totalDD is seen at 0.5 cycles for an amount of strain so close to the as-received, likely due to noise or error in post-processing, so the other cycle numbers will be primarily emphasized.

The totalDD data suggest a general increase in dislocation density as function of strain (i.e., number of cycles). As-received totalDD is significantly lower than after incurred strain, as expected. TotalDD in the unbent region is generally higher than in the bent region, aligning with previous observations, due to overall increased amounts of strain. Note that the first data point, bent and unbent, for 8 and 12 cycles lies within the simulated bottom ratcheting region, and the second in the pure tension region. Both datapoints for 1 cycle are within the simulated bottom ratcheting region, making their response slightly more uniform. An increase in dislocation density toward the middle of the sheet is seen at 8 cycles in both regions, as in the GND case, indicating some dislocation annihilation from reverse loading in the bottom ratcheting zone compared to higher accumulation in the tension zone. At 12 cycles, in the bent region there is some increase in totalDD shifting from the ratcheting into the tension region, like the GND data, expected to decrease approximately linearly toward the top surface of the sheet. In the unbent region indications of a general decrease toward the top surface are observed, where the most accumulation is expected near the bottom surface due, in this case, to top-and-bottom roller configuration asymmetry, in agreement with the unbent GND data. Again, applied axial tension combined with tensile bending induces compounded amounts of tensile stress and subsequent plastic deformation near the surfaces, so net higher accumulation at the bottom *surface* near failure is unsurprising, taking saturation behavior into account. Observations of dislocation saturation from this data are less obvious with only a few data points per cycle.

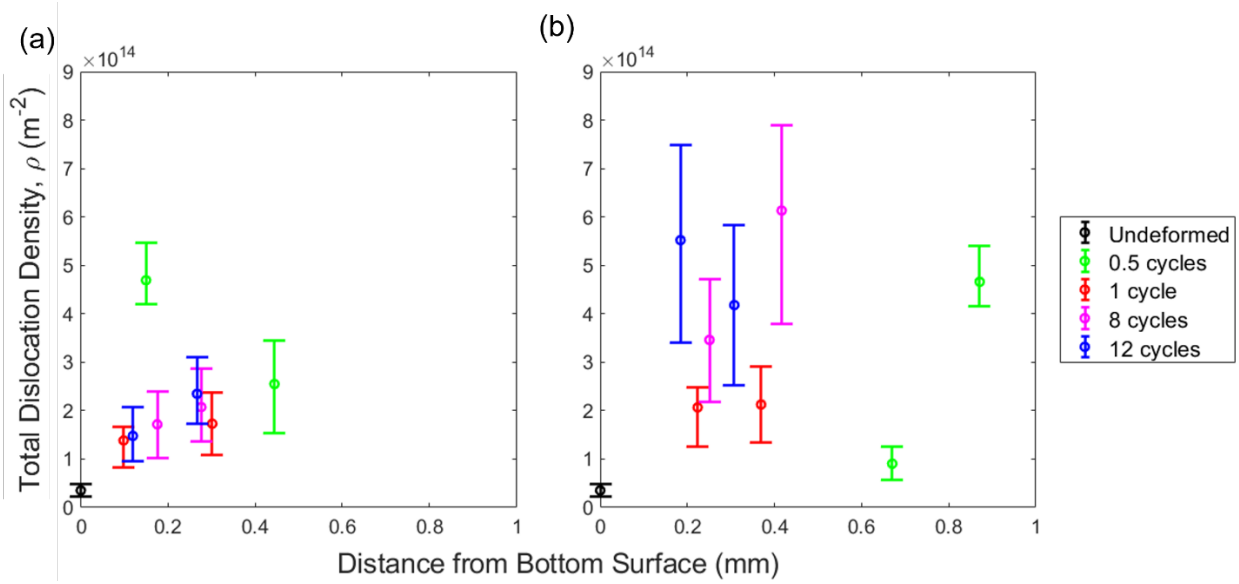

Figure 12. ND totalDD accumulation in the (a) bent region and (b) unbent region, with error representing the offset from the optimum value reached (minimized WSSR). Data for each cycle is centered at 0.5mm. For 0.5 cycles in the unbent region, data was also collected near the top surface of the sheet.

Average dislocation densities across the sheet thickness summarizing and comparing CMWP and HR-EBSD measurements are shown in Figure 13, with values listed in Tables A.1-2 of the Appendix. Note that the averages for CMWP consist of a small sample size of two data

points, so only mean and standard deviation are reported, and broader statistical tools are not employed. The values for totalDD are normally expected to be higher than those for GND density since the latter is a subcomponent of the total, but, as was previously mentioned, noise and inherent differences between the two characterization methods offset "true" dislocation density values relative to each method. Sample faces analyzed (TD vs. ND) were also different. Inferences from *trends* observed in the data from the two characterization procedures are, therefore, reported. For both the GND and totalDD data, the undeformed (as-received) dislocation density was significantly lower than regions that had been strained (GND: 1.41×10^{14} m^{-2}; CMWP: 0.353×10^{14} m^{-2}), serving as a check of coherence and reference for initial dislocation content. Some similar trends are observed between the two characterization methods, namely that dislocation density in the 3x (unbent) region is higher than in the bent region leading up to failure, and that dislocation density generally increases with increasing number of cycles (i.e., strain). General dislocation density values obtained, having magnitudes of [$\times10^{13}$] to [$\times10^{15}$], are realistic relative to typical values in rolled and/or heavily deformed polycrystalline metals.

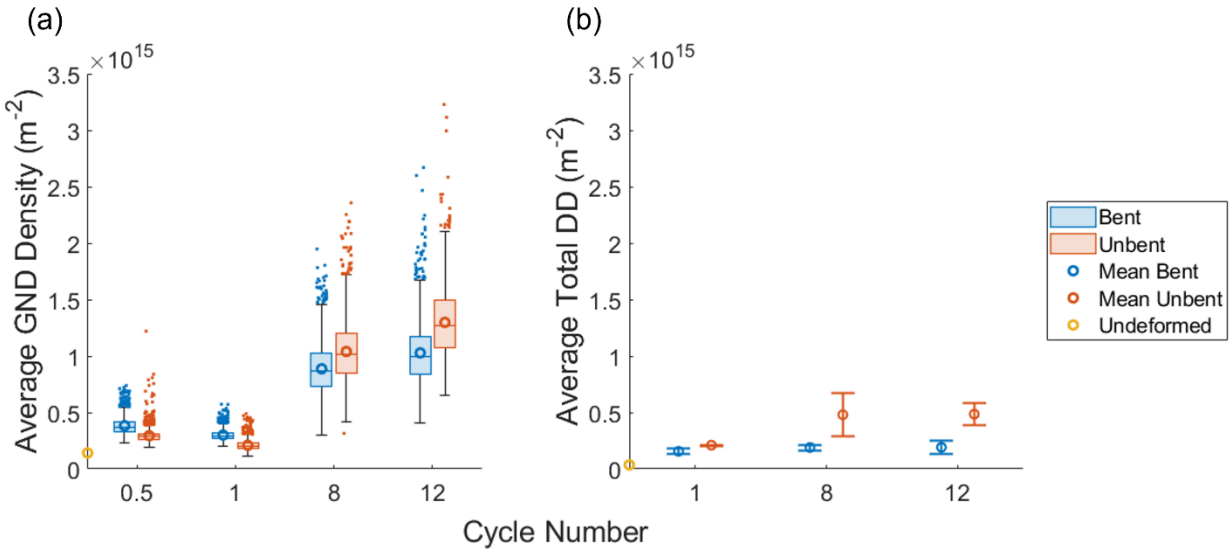

Figure 13. (a) Average GND density and (b) average totalDD accumulation in the bent and unbent regions for relevant experimental cycle numbers. Due to having only 2 datapoints in each dataset, boxplots are foregone in (b) and plotted rather as means and standard deviations. 0.5-cycle data from CMWP was omitted from the comparison.

3.4 Discussion of dislocation influence on enhanced RT ETF

To expand the discussion of evolving distributions of dislocations with increasing cycles in CBT, phenomenological deformation mechanisms of cyclic loading and reversed dislocations are considered. Cyclic deformation (e.g., tension-to-compression or compression-to-tension) relies on a combination of isotropic and kinematic hardening laws [37]. Reverse isotropic hardening is influenced by the extent of dislocation annihilation during reverse loading, leading to a decrease in overall dislocation content. Reverse kinematic hardening is influenced by the release of accumulated backstresses during reverse loading on the slip-system level. Considering the influence of both laws in plasticity models has shown that cyclic loading is often accompanied

by a permanent softening effect, or decreased hardening rate during reverse loading to large strains, subsequent drop in yield stress, and offsetting of forward and reverse flow stresses [38, 39]. In terms of the isotropic hardening contribution, dislocations accumulate in the forward strain path, and a certain percentage of them are annihilated in the reverse direction (i.e., during reverse glide) as slip/loading directions are reversed. Specifically, a percentage of loosely tangled dislocations contained in or around organized dislocation substructures (e.g., cell walls and block boundaries) and certain substructures themselves formed during the primary deformation path annihilate in the reverse direction [38, 40]. New dislocation substructures simultaneously form during the reverse deformation. Thus, reversible dislocation motion and annihilation heavily influence hardening and hardening rates during cyclic loading [39], and cellular structures can persist throughout [23]. Note that such structures have been shown to be favored under cyclic loading with a positive mean stress, such as in additive positive constant tension and positive bending of CBT, where the complex stress states promote multiple slip [18, 23, 41]. Significant accuracy improvements of elasto-plastic self-consistent (EPSC) model predictions of experimental data for reverse loading behavior of cyclically deformed samples in AA6022-T4, DP590 steel, CP-Ti Grade 2, and others have been achieved by incorporating reversible dislocation mechanisms alongside backstresses and inter-granular residual stresses [39, 40, 42].

CBT deformation differs from pure cyclic loading, however, since the cyclic bending is superimposed with macroscopic tension [23]. Nonetheless, the discussed principles of reverse annihilation of dislocations apply to CBT in the bending/unbending regions of the sheet thickness since they, indeed, undergo cyclically reversing tension-to-compression or compression-to-tension bending stress states. In particular, dislocations and dislocation substructures accumulate in the ratcheting region near the top surface of the sheet in a state of tensile bending as the first roller passes, and a certain percentage annihilate during reverse compressive bending as the next roller passes. This results in delayed hardening in the ratcheting portions of the sheet, inherently reducing the amount of dislocation development in those areas compared to the middle tension zone. Determining which strain path has a higher hardening rate is thereby essential to determining which loading direction (positive or negative, tensile or compressive bending in the case of the ratcheting zones) will have the greater percentage of reversed dislocations.

The CP-Ti Grade 4 sheet from this work exhibits compressive-tensile yield stress asymmetry in the RD, with compressive yield strength being highest in that direction, but nearly symmetric yield strengths in the TD; it also exhibits a higher monotonic compressive hardening rate (compared to the monotonic tension hardening rate) in both RD and TD directions. Increased compressive hardening rates were also observed in CP-Ti Grades 1 [43] and 2 [44], as well as early re-yielding in cyclic loading. Recall that the key difference between Grades 1 through 4 is increasing amounts of iron and oxygen content (solid solution strengthening), so most of the same deformation mechanisms are active but at differing degrees. Accordingly, an EPSC crystal plasticity model of the Grade 2 data found that relative amounts of slip (i.e., prismatic, basal, and pyramidal modes) for strains up to 10% were consistent whether under monotonic or reverse loading, compression or tension, compression-to-tension or tension-to-compression, with prismatic being the dominant slip mode [45]. The model also showed favorable pyramidal⟨c+a⟩ slip over twinning in the reverse loading path during cyclic loading. Additional cyclic modeling of AA6022-T4 added the insight that in that material there was not a significant difference in relative amounts of slip between ST and CBT [10]. This could be similarly inferred for CP-Ti,

indicating consistent relative amounts of slip through the thickness when the loading direction is the same.

Additional insights can be gained from the simulated axial plastic strain (Figure 7). In pre-necking ST, the axial plastic strain is expected to be relatively uniform, whereas in CBT the simulation predicts it to generally be highest at the sheet surfaces. This would normally predict higher dislocation accumulation in those regions, but since the model does not account for reversible dislocations, the simulated axial plastic strain includes the added accumulation from positive and negative loading. A percentage of dislocations would normally cancel during strain in opposite loading directions from reverse bending near the surfaces. Therefore, the experimental results above showing a *decrease* in dislocation accumulation in surface regions of cyclic loading can then attribute the decrease to reverse dislocation motion and annihilation.

In summary, recall that ~80% of the additional elongation afforded in CBT compared to ST was attributed to delayed necking, the primary mechanism. The goal was then to investigate through-thickness dislocation evolution as a secondary mechanism of enhanced ETF. Relating all of this to especially the 8-cycle dislocation density distributions (Figures 9, 10, and 12), exhibiting notable increases in the sheet center, delayed hardening was plainly observed in the ratcheting portions of the sheet. Therefore, it is proposed that additional secondary ductility (i.e., ETF) extension during CBT in CP-Ti Grade 4 is attributed, in part, to slowed dislocation (i.e., damage) accumulation due to reverse dislocation motion and underlying annihilation in the strain path reversal, ratcheting regions of the sheet. This is influenced by an increased hardening rate in compression and early re-yielding during cyclic deformation. The applied tension causes a higher overall rate of dislocation accumulation in the pure tension region of the sheet (Figure 11), with delayed hardening in the ratcheting portions owing to a complex evolution of dislocation accumulation and annihilation, together with relevant formation and complete or partial dissolution of dislocation cells and cell block boundaries. As the ratcheting region shrinks and the sheet progressively thins and hardens leading up to failure, the amount of annihilation from reverse dislocation motion that can take place in the ratcheting regions diminishes, leading to eventual dislocation saturation. At the point of failure, the highest dislocation density in the processing region is at the bottom sheet surface, where the asymmetric roller configuration has induced a significant amount of net tensile plastic deformation near the surface from combined positive bending and applied tension.

In short, the CBT process provides deformation mechanisms in sheet forming that slow dislocation accumulation via cyclic bending in the regions of highest expected stress (i.e., the surfaces), concentrating accumulation in the center, thereby affording more total strain than in ST and enhancing achievable ETF. Sheet thinning and subsequent shrinking of ratcheting (cyclic) zones develops increased central damage accumulation as the amount of stabilizing compression decreases. Thus, getting the most extended ETF from the CBT process may be partially achieved by concentrating efforts in design, material selection, and processing (e.g., diameter of the rollers) such as to maintain constant width of the ratcheting regions for as long as possible; in this material, for example, this would mean attempting to maintain each ratcheting zone at ~40% of the thickness with only 20% being in tension.

3.5 Relationship between dislocation evolution and void formation

The reported findings on dislocation evolution are corroborated by damage evolution near failure in the sense of *voids* in CP-Ti Grade 4 recently reported in a parallel study [6]. It was determined that voids form at similar exponential rates (with respect to strain) for both CBT and ST. Isolated

data from this study from the 3x (unbent) region at 9, 11, and 12 cycles is shown in Figure 14. At 9 cycles, the void density distribution is relatively uniform, and eventually increases in the center of the sheet approaching failure (recall that failure occurs at ~12.5 cycles). The same trend was observed in samples taken from the 2x/3x interface, the common failure point of most specimens, indicating that, throughout the gauge length, voids likely concentrate in the sheet center leading up to failure. The void density was 2x higher in the middle than at the surfaces in CBT, and 2.5x higher in ST. Notably, the GND density in the 3x (unbent) region was highest in the center of the sheet at 8 cycles (Figure 10) and the totalDD also increased toward the center (Figure 12), suggesting that the significant increase in dislocations in the middle of the sheet at *8* cycles *precedes* void formation (in the size range visible to CT) in the middle of the sheet, which occurs between 9 and 11 cycles.

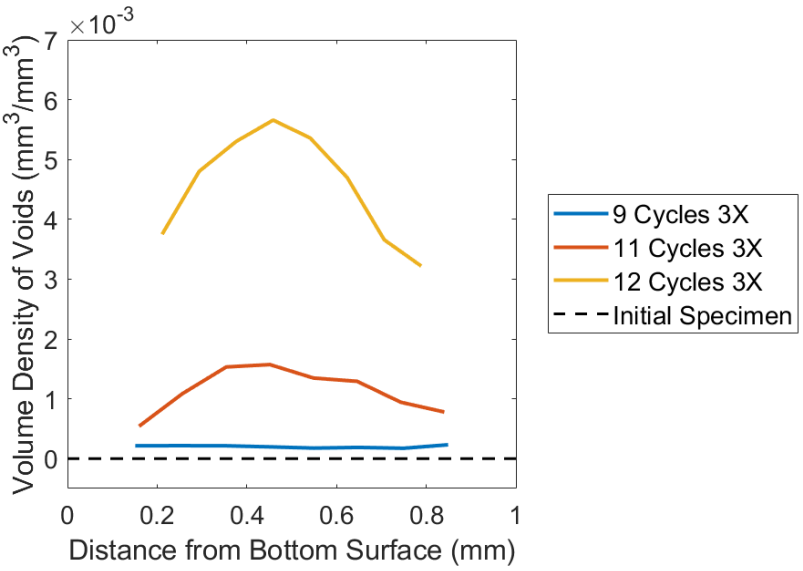

Figure 14. 3x (unbent) region through-thickness void volume density data for 9, 11, and 12 (out of ~12.5) cycles relative to the as-received material. This image was adapted from original data found in [6].

It has been shown that in ductile fracture of pure metals, voids typically form via vacancy condensation as the primary mechanism: dislocation cell walls and cell block boundaries created by plastic deformation facilitate vacancy condensation by increasing hydrostatic stress concentration, causing nucleation of voids [46-48]. Vacancy concentration and hydrostatic stress reduce the activation free energy of void nucleation, and dislocation cell walls increase hydrostatic stresses, thus making void nucleation more favorable. As a result, vacancy condensation causes most voids to nucleate in regions of high dislocation density, and the voids then grow by consuming dislocations from the bulk [47]. The nature of the material of interest, being shown to fail with ductile fracture [6] and being 99.97% (i.e., highly pure) α-titanium, suggests that the conditions for activation of this void formation mechanism are satisfied despite its hexagonal structure.

In materials that deform by twinning, both pure and those containing second-phase particles, voids can also nucleate at grain boundary/twin intersections and/or twin/twin

intersections, which act as high stress concentrations [48]. It was correspondingly observed that voids in high-purity α-Ti often nucleate at the intersection between T_1 (primary) and T_2 (secondary) tensile twins [48, 49]. Although incipient voids were not characterized relative to twins and grain boundaries with EBSD in this or the overlapping study, the lack of overall twinning observed in the supplied material supports the assumption that void formation and growth principally occur by vacancy condensation at dislocation boundaries, in regions of high dislocation density.

Based on the previous discussion, it is assumed that dislocation density accumulation in the sheet rises in the sheet center (due to the constantly tensile nature of the stress, as opposed to cyclical stress near the sheet edges), along with the greater stress triaxiality observed in the simulations of CBT, results in a faster rate of void nucleation. These would not initially be observed in the CT scans, due to resolution limits, but would become visible as they continue to grow at a later number of cycles. At 12 cycles the apparent trends were reversed, where void density peaked at the center and the dislocation density distribution was linear and greatest at the surface (the latter bias, once again, likely due to roller configuration asymmetry). Pitkin et al. [6] reported that the voids continued to form with little growth leading up to crack initiation and failure, concentrating in the middle of the sheet. The dislocations, on the other hand, saturated throughout the sheet close to failure, with the density increasing near the surfaces. This subsequently influenced a sharp increase in the void density, including near the sheet surfaces, between 11 and 12 cycles (Figure 14), while remaining highest in the central tensile region where dislocation density was formerly highest. Therefore, in terms of damage evolution in CBT, high dislocation density development in the pure tension region of the sheet thickness approaching failure precedes and imparts nucleation sites for voids, causing them to nucleate and concentrate also in the sheet center. Cyclic bending/unbending in the ratcheting portions of the sheet delay hardening in those areas, forcing voids to form and the distribution to concentrate in the center where there exists a high accumulation of dislocations and (likely) dislocation cells and cell block boundaries.

A high amount of central damage (i.e., accumulation of both dislocations and voids) is evidenced by analysis of the fracture surfaces in CBT. The specimen fracture surfaces were found to be essentially perpendicular to the loading direction, with the CP-Ti having only small shear lips [4-6]. This supports the observation of significant void accumulation in the sheet center before fracture. Note that in both TRIP steels and CP-Ti Grade 4, stress triaxiality in CBT is generally highest in the middle of the sheet. Thus, incremental and reversal deformation effects of CBT that concentrate damage accumulation toward the center of the sheet, away from peak surface stresses, are presumably able to extend ETF at RT in CP-Ti, with dislocations and voids playing an *interrelated* and *sequential* role.

4. Conclusions

Using CBT to process CP-Ti Grade 4 has yielded up to three times enhanced ETF compared to ST, where ~80% (i.e., most) of the extended ETF is attributed to delayed localization from cyclic, incremental deformation/elongation. Stabilizing compressive stress profiles and relaxations of mechanical strain field fields are secondary contributions to the improved elongation. Microscale defect structures and damage accumulation contribute additional secondary effects and are essential in explaining deformation mechanisms to exploit the elongation-enhancing effects of CBT. This study tracked dislocation development through the sheet thickness throughout the CBT process in CP-Ti Grade 4 to determine if, as a secondary

mechanism to improved ETF, dislocation evolution was slower in the bending/unbending (ratcheting) portions of the sheet. Dislocation content was characterized with HR-EBSD and XRD-based CMWP via interrupted testing on two regions of interest – directly under the middle roller and in the 3x region once rollers had passed – at 0.5, 1, 8, and 12 cycles, where failure typically occurs at ~12.5 cycles. Tracking dislocation evolution in both bent (1x/2x) and unbent (3x, processing) regions revealed content and distribution of dislocation density representative of the current deformation zone and the main CBT processing region, respectively. Results obtained allow the following main conclusions to be drawn:

- Damage in the sense of dislocation accumulation occurs more slowly in the ratcheting portions of the sheet (i.e., near the surfaces) from cyclic load reversals, and develops faster in the central tensile portion of the sheet. Indeed, dislocation density was shown to generally accumulate 1.21x faster in ST than in CBT. During the CBT process, dislocation density is relatively uniform across the sheet at lower cycles, increases in the sheet center at higher cycles, and eventually approaches saturation near failure both immediately under the middle roller and in the (3x) processing region. At 8 cycles, dislocation densities in the bent and unbent regions were found to be 1.43x and up to 1.32x higher, respectively, in the middle of sheet compared to near the surfaces, exhibiting a quadratic relationship with respect to depth into the sheet. This is attributed to reverse dislocation motion and underlying annihilation of dislocations from cyclic bending/unbending in the ratcheting zones. At 12 cycles, right before failure, the relationship is once again approximately linear, indicating that dislocation density is approaching saturation throughout the sheet.
- Dislocation content in the unbent region was highest near the bottom surface of the sheet near failure, owing to roller configuration asymmetry (i.e., one on top, two on bottom) in conjunction with the highest amount of plastic deformation occurring near the surfaces from superimposed tensile bending and macroscopically applied tensile stress. Unbending/straightening and relaxation of the sheet as rollers passed produced a more uniform (i.e., less steep) distribution of dislocation densities throughout the process compared to the bent region, indicating delayed localized concentration of damage near the surfaces via dislocation reversal and annihilation. As expected, dislocation density was largest in the unbent region at higher cycles compared to the bent region from higher overall induced strain.
- An increase in dislocation density in the middle of the sheet (relative to the sheet surfaces) after 8 cycles precedes (and presumably causes) significant nucleation and growth of voids in the sheet center between 9 and 11 cycles observed in a parallel study [6]. Concentrated damage in the middle of the sheet, away from peak stresses near the surfaces, presumably contributes to delayed failure in CBT.

Acknowledgements
This work is based upon a project supported by the National Science Foundation under GOALI grant CMMI -2147126 (BYU) and -2147122 (UNH). CP-Ti Grade 4 sheets were supplied by Boeing. The authors would like to acknowledge Tamas Ungár (CMWP), Stacey Smith (BYU X-Ray Diffraction Facility), and Felipe Rivera (BYU Electron Microscopy Facility) for providing access to invaluable expertise and equipment that allowed key parts of this project to be performed. The authors would also like to acknowledge Sarah Sanderson (BYU), Asher Webb (BYU), and Addison McClure (BYU) for experimental support.

Appendix

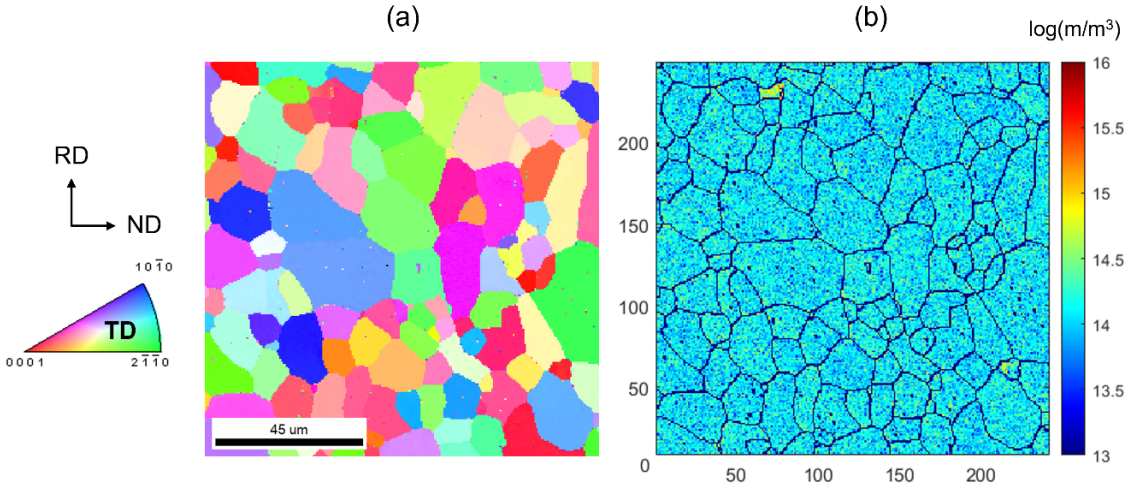

Figure A.1. (a) Uncleaned EBSD inverse pole figure (IPF) map with corresponding (b) GND density map of the as-received CP-Ti Grade 4 sheet.

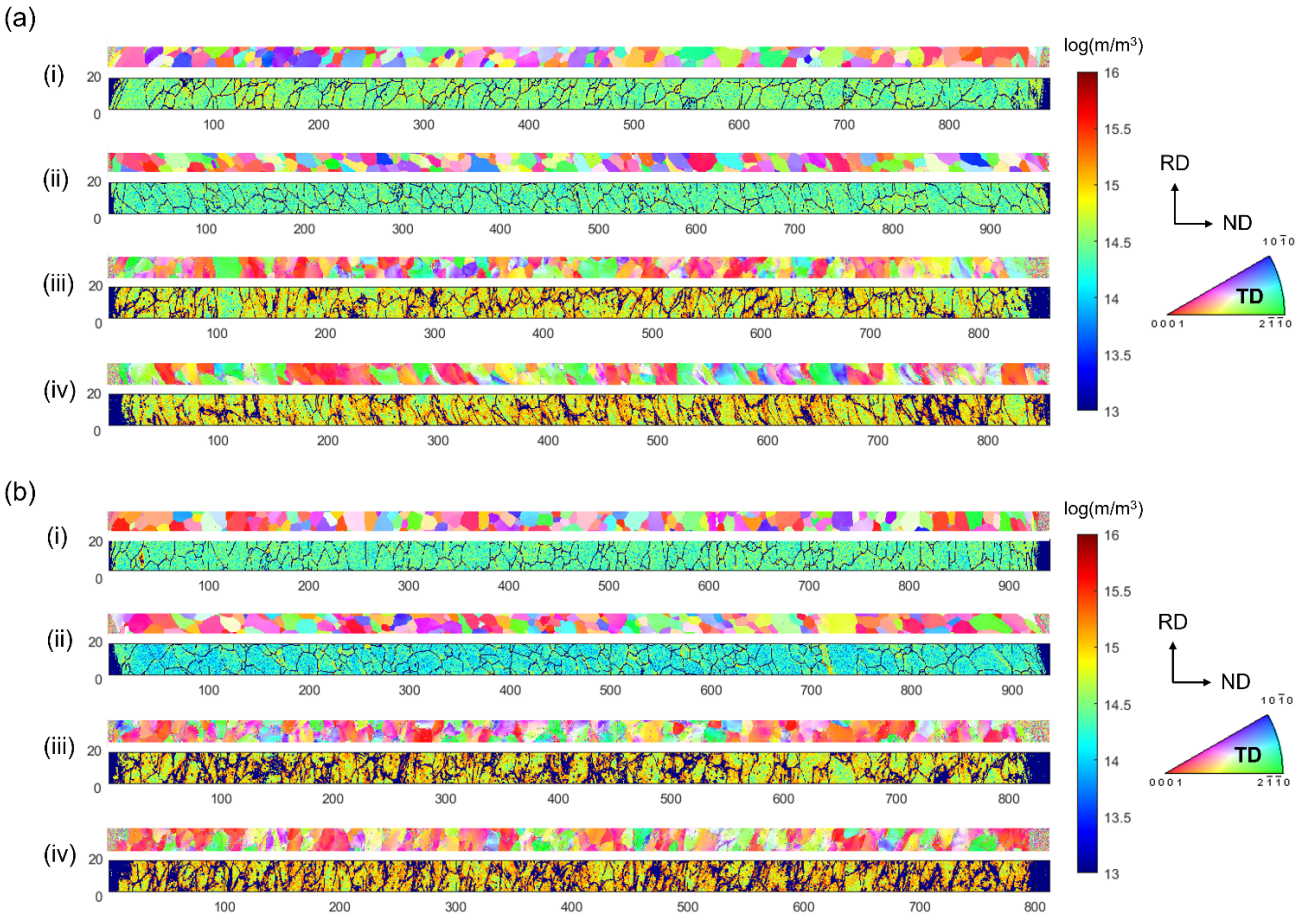

Figure A.2. Corresponding (top) uncleaned EBSD inverse pole figure (IPF) maps and (bottom) GND density maps through the sheet thickness in the (a) bent and (b) unbent regions at (i) 0.5, (ii) 1, (iii) 8, and (iv) 12 cycles.

Table A.1. Average through-thickness GND density values corresponding to maps in Figures A.1-2 and the average dislocation density plot in Figure 13.

	Avg. GND Density (m/m^3)	
Undeformed	1.411×10^{14}	
Cycle No.	Bent Region	Unbent Region
0.5	3.784×10^{14}	2.904×10^{14}
1	2.977×10^{14}	2.071×10^{14}
8	8.721×10^{14}	1.008×10^{15}
12	9.935×10^{14}	1.252×10^{15}

Table A.2. Average through-thickness total dislocation density values corresponding to the average dislocation density plot in Figure 13.

	Avg. Total Dislocation Density (m/m^3)	
Undeformed	0.353×10^{14}	
Cycle No.	Bent Region	Unbent Region
1	1.557×10^{14}	2.096×10^{14}
8	1.895×10^{14}	4.796×10^{14}
12	1.912×10^{14}	4.851×10^{14}

References

[1] H.W. Swift, Plastic bending under tension, Engineering 166 (1948) 333-359.
[2] T.J. Roemer, T.J. Barrett, M. Knezevic, B.L. Kinsey, Y.P. Korkolis, Experimental study of continuous-bending-under-tension of AA6022-T4, Journal of Materials Processing Technology 266 (2019) 707-714.
[3] C.M. Poulin, Y.P. Korkolis, B.L. Kinsey, M. Knezevic, Over five-times improved elongation-to-fracture of dual-phase 1180 steel by continuous-bending-under-tension, Materials & Design 161 (2019) 95-105.
[4] R. Sharma, C.M. Poulin, M. Knezevic, M.P. Miles, D.T. Fullwood, Micromechanical origins of remarkable elongation-to-fracture in AHSS TRIP steels via continuous bending under tension, Materials Science and Engineering: A 825 (2021) 141876.
[5] N. Matukhno, N. Kljestan, M. Knezevic, Enhancing elongation and trading off strength versus ductility of commercially pure titanium sheets using cyclic bending under tension and annealing, International Journal of Solids and Structures 276 (2023) 112324.
[6] P.N. Nicholas Pitkin, David T. Fullwood, Marko Knezevic, Damage evolution and ductile fracture of commercially-pure titanium sheets subjected to simple tension and cyclic bending under tension, Journal of Materials Research and Technology (In Press) (2024).
[7] N. Matukhno, N. Kljestan, S.C. Vogel, M. Knezevic, Cyclic bending under tension of alloy AZ31 sheets: Influence on elongation-to-fracture and strength, Materials Science and Engineering: A 857 (2022) 144127.
[8] N. Matukhno, N. Kljestan, S.C. Vogel, M. Knezevic, Improvements in elongation and tradeoffs in strength and ductility of several Mg sheet alloys through cyclic bending under tension and annealing, International Journal of Material Forming 16(5) (2023) 52.
[9] T.J. Barrett, S. Takagi, N. Islam, T. Kuwabara, T. Hassan, B.L. Kinsey, M. Knezevic, Y.P. Korkolis, Material modeling and simulation of continuous-bending-under-tension of AA6022-T4, Journal of Materials Processing Technology 287 (2021) 116658.
[10] M. Zecevic, M. Knezevic, Origins of improved elongation to fracture in cyclic bending under tension of AA6022-T4 sheets as revealed using crystal plasticity modeling, Mechanics of Materials 177 (2023) 104546.
[11] T.J. Barrett, M. Knezevic, Modeling material behavior during continuous bending under tension for inferring the post-necking strain hardening response of ductile sheet metals: Application to DP 780 steel, International Journal of Mechanical Sciences 174 (2020) 105508.
[12] T.M.T. Oishi, N. Pitkin, N. Miller, D. Mensah, D.T. Fullwood, M.P. Miles, B.L. Kinsey, M. Knezevic, Influence of specimen width on the elongation-to-fracture in cyclic-bending-under-tension of commercially pure titanium sheets, International Journal of Mechanical Sciences 278 (2024) 109447.
[13] W.C. Emmens, A.H. van den Boogaard, Cyclic stretch-bending: Mechanics, stability and formability, Journal of Materials Processing Technology 211(12) (2011) 1965-1981.
[14] K. Yaddanapudi, M. Knezevic, S. Mahajan, I.J. Beyerlein, Plasticity and structure evolution of ferrite and martensite in DP 1180 during tension and cyclic bending under tension to large strains, Materials Science and Engineering: A 820 (2021) 141536.
[15] N. Bosh, C. Müller, H. Mozaffari-Jovein, Deformation twinning in cp-Ti and its effect on fatigue cracking, Materials Characterization 155 (2019) 109810.
[16] T. Wang, B. Li, M. Li, Y. Li, Z. Wang, Z. Nie, Effects of strain rates on deformation twinning behavior in α-titanium, Materials Characterization 106 (2015) 218-225.

[17] Y.B. Chun, S.H. Yu, S.L. Semiatin, S.K. Hwang, Effect of deformation twinning on microstructure and texture evolution during cold rolling of CP-titanium, Materials Science and Engineering: A 398(1-2) (2005) 209-219.
[18] M.-S. Lee, J.-R. Lee, J.B. Jeon, J.W. Won, Y.-T. Hyun, T.-S. Jun, In-situ study of anisotropic strain-hardening and grain boundary mediated deformation in commercially pure titanium, Journal of Materials Research and Technology 24 (2023) 5389-5403.
[19] N. Yi, T. Hama, A. Kobuki, H. Fujimoto, H. Takuda, Anisotropic deformation behavior under various strain paths in commercially pure titanium Grade 1 and Grade 2 sheets, Materials Science and Engineering: A 655 (2016) 70-85.
[20] S.-W. Choi, J.S. Jeong, J.W. Won, J.K. Hong, Y.S. Choi, Grade-4 commercially pure titanium with ultrahigh strength achieved by twinning-induced grain refinement through cryogenic deformation, Journal of Materials Science & Technology 66 (2021) 193-201.
[21] Y.F. Yang, Z.R. He, J. Ma, H. Yang, J.Y. Min, S.L. Zang, H. Li, Evolving asymmetric and anisotropic hardening of CP-Ti sheets under monotonic and reverse loading: Characterization and modeling, International Journal of Plasticity 159 (2022) 103445.
[22] R.R. Boyer, An overview on the use of titanium in the aerospace industry, Materials Science and Engineering: A 213(1-2) (1996) 103-114.
[23] M. Knezevic, C.M. Poulin, X. Zheng, S. Zheng, I.J. Beyerlein, Strengthening of alloy AA6022-T4 by continuous bending under tension, Materials Science and Engineering: A 758 (2019) 47-55.
[24] O. Muránsky, L. Balogh, M. Tran, C.J. Hamelin, J.S. Park, M.R. Daymond, On the measurement of dislocations and dislocation substructures using EBSD and HRSD techniques, Acta Materialia 175 (2019) 297-313.
[25] M.F. Ashby, The deformation of plastically non-homogeneous materials, The Philosophical Magazine: A Journal of Theoretical Experimental and Applied Physics 21(170) (1970) 399-424.
[26] T.J. Ruggles, D.T. Fullwood, Estimations of bulk geometrically necessary dislocation density using high resolution EBSD, Ultramicroscopy 133 (2013) 8-15.
[27] K. Ekkehart, Continuum theory of dislocations and self-stresses, (1958).
[28] J.F. Nye, Some geometrical relations in dislocated crystals, Acta Metallurgica 1(2) (1953) 153-162.
[29] T.J. Ruggles, T.M. Rampton, A. Khosravani, D.T. Fullwood, The effect of length scale on the determination of geometrically necessary dislocations via EBSD continuum dislocation microscopy, Ultramicroscopy 164 (2016) 1-10.
[30] T.J. Ruggles, J.I. Deitz, A.A. Allerman, C.B. Carter, J.R. Michael, Identification of Star Defects in Gallium Nitride with HREBSD and ECCI, Microsc Microanal 27(2) (2021) 257-265.
[31] G. Ribárik, Modeling of diffraction patterns based on microstructural properties, Eötvös Loránd University (2008).
[32] I.C. Dragomir, T. Ungár, Contrast factors of dislocations in the hexagonal crystal system, J Appl Crystallogr 35(5) (2002) 556-564.
[33] U. Essmann, H. Mughrabi, Annihilation of dislocations during tensile and cyclic deformation and limits of dislocation densities, Philosophical Magazine A 40(6) (1979) 731-756.
[34] J.W. Hutchinson, Plastic stress-strain relations of F.C.C polycrystalline metals hardening according to Taylor's rule, Journal of the Mechanics and Physics of Solids 12(1) (1964) 11-24.
[35] M. Madrid, C. Vantyne, S. Sriram, E. Pavlina, J. Hu, K. Clarke, Hole expansion ratio in intercritically annealed QP 980/1180 steel grades as a function of testing condition, IOP Conference Series: Materials Science and Engineering 418 (2018) 012083.

[36] T. Ruggles, S. Cluff, M. Miles, D. Fullwood, C. Daniels, A. Avila, M. Chen, Ductility of advanced high-strength steel in the presence of a sheared edge, Jom 68 (2016) 1839-1849.
[37] S. Daroju, T. Kuwabara, R. Sharma, D.T. Fullwood, M.P. Miles, M. Knezevic, Experimental characterization and crystal plasticity modeling for predicting load reversals in AA6016-T4 and AA7021-T79, International Journal of Plasticity 153 (2022) 103292.
[38] T. Hasegawa, T. Yakou, S. Karashima, Deformation behaviour and dislocation structures upon stress reversal in polycrystalline aluminium, Materials Science and Engineering 20 (1975) 267-276.
[39] M. Zecevic, M. Knezevic, A dislocation density based elasto-plastic self-consistent model for the prediction of cyclic deformation: Application to AA6022-T4, International Journal of Plasticity 72 (2015) 200-217.
[40] M. Zecevic, Y.P. Korkolis, T. Kuwabara, M. Knezevic, Dual-phase steel sheets under cyclic tension–compression to large strains: Experiments and crystal plasticity modeling, Journal of the Mechanics and Physics of Solids 96 (2016) 65-87.
[41] P. Lukáš, L. Kunz, Cyclic plasticity and substructure of metals, Materials Science and Engineering: A 322(1) (2002) 217-227.
[42] M. Zecevic, M. Knezevic, I.J. Beyerlein, C.N. Tomé, An elasto-plastic self-consistent model with hardening based on dislocation density, twinning and de-twinning: Application to strain path changes in HCP metals, Materials Science and Engineering: A 638 (2015) 262-274.
[43] J.L.W. Warwick, N.G. Jones, K.M. Rahman, D. Dye, Lattice strain evolution during tensile and compressive loading of CP Ti, Acta Materialia 60(19) (2012) 6720-6731.
[44] T. Hama, H. Nagao, A. Kobuki, H. Fujimoto, H. Takuda, Work-hardening and twinning behaviors in a commercially pure titanium sheet under various loading paths, Materials Science and Engineering: A 620 (2015) 390-398.
[45] J. Wang, M. Zecevic, M. Knezevic, I.J. Beyerlein, Polycrystal plasticity modeling for load reversals in commercially pure titanium, International Journal of Plasticity 125 (2020) 294-313.
[46] P. Yang, P. Zhao, Void nucleation at dislocation boundaries aided by the synergy of multiple dislocation pile-ups, International Journal of Plasticity 171 (2023) 103779.
[47] P. Noell, J. Carroll, K. Hattar, B. Clark, B. Boyce, Do voids nucleate at grain boundaries during ductile rupture?, Acta Materialia 137 (2017) 103-114.
[48] P.J. Noell, R.B. Sills, A.A. Benzerga, B.L. Boyce, Void nucleation during ductile rupture of metals: A review, Progress in Materials Science 135 (2023) 101085.
[49] T.R. Bieler, P. Eisenlohr, C. Zhang, H.J. Phukan, M.A. Crimp, Grain boundaries and interfaces in slip transfer, Current Opinion in Solid State and Materials Science 18(4) (2014) 212-226.